applied sciences

MDPI

Article

Aerodynamic Window Sealing of a Large-Aperture Channel for High-Power Laser Transmission

Xunqing Huang [1,2], Yunhan Wu [1,2], Yingzhong Shi [1,2] and Shuai Shao [1,*]

[1] State Key Laboratory of Laser Interaction with Matter, Changchun Institute of Optics, Fine Mechanics and Physics, Chinese Academy of Sciences, Changchun 130033, China; huangxunqing19@mails.ucas.ac.cn (X.H.); wuyunhan1220@163.com (Y.W.); ciompsyz@163.com (Y.S.)
[2] University of Chinese Academy of Sciences, Beijing 100049, China
* Correspondence: sshuaiciomp2021@163.com

Abstract: In this study, the sealing of a large-aperture channel for high-power laser transmission is achieved using an aerodynamic window. Further, a numerical model of the gas and dust particle motion in the channel is established under three different blowing schemes, and the sealing performance of the large-aperture channel is analyzed and compared under different blowing schemes. The results indicate that the larger the proportion of purge gas volume flows in the axial direction, the better the sealing effect of the channel. More importantly, the axial blowing scheme can ensure that the large-aperture channel maintains the relative positive pressure to the external environment, effectively blocking the ambient gas and dust particles blowing in. The axial blowing scheme can achieve the sealing requirements of the large-aperture channel in an environment where the ambient wind speed is less than 20 m/s, and the dust particle mass concentration is less than 8×10^{-3} kg/m^3. In this case, the minimum non-zero z-directional wind speed is stable and positive at a position 100 mm away from the port in the channel, and the particle mass concentration is zero.

Keywords: large-aperture channel sealing; aerodynamic window; wind speed; dust particle mass concentration

check for updates

Citation: Huang, X.; Wu, Y.; Shi, Y.; Shao, S. Aerodynamic Window Sealing of a Large-Aperture Channel for High-Power Laser Transmission. *Appl. Sci.* **2022**, *12*, 7301. https://doi.org/10.3390/app12147301

Academic Editor: Jianzhong Lin

Received: 19 May 2022
Accepted: 15 July 2022
Published: 20 July 2022

Publisher's Note: MDPI stays neutral with regard to jurisdictional claims in published maps and institutional affiliations.

Copyright: © 2022 by the authors. Licensee MDPI, Basel, Switzerland. This article is an open access article distributed under the terms and conditions of the Creative Commons Attribution (CC BY) license (https://creativecommons.org/licenses/by/4.0/).

1. Introduction

High-power laser emission equipment can be carried on cars, ships, and aircraft. Transmitting in a large-aperture channel makes the laser free to change the direction of the beam for better tracking a target, which is extensively used in military and manufacturing applications [1–3]. In the process of high-power laser transmission, the aerosol particles in the external environment absorb part of the laser energy, which increases the local temperature in the large-aperture channel, producing thermal blooming [4–6]. When aerosol particles are attached to the surface of optical elements, irradiation by a high-power laser will cause irreversible effects, such as component damage [7,8]. Therefore, it is crucial to ensure that the gas in the channel is in a dry and clean state [9]. The aerodynamic window sealing method was adopted to continuously transport purge gas to the large-aperture channel and utilize the incompressibility of the gas to maintain the pressure difference between the inside and outside of the channel, realizing the blocking of ambient air and dust particles into the interior of the channel.

With the increasing applications of lasers, there have been many studies on the window sealing of laser transmitting channels. The literature covers the use of crystal lenses for window sealing and the analysis of mechanical, thermal, and optical properties of crystalline materials as optical windows by considering the absorption dissipation and thermo-optical coefficients of different crystalline materials [10–12]. Mineral acid leaching and HF-based etching technology have been employed to mitigate the laser damage precursor in the subsurface of crystal lenses to enhance the laser-induced damage resistance [13].

The reflection loss for spinel was reduced from 7% per surface to 0.9% by applying anti-reflection surface structures (ARSS) to the crystalline material, and for fused silica with ARSS, the reflection loss was reduced to 0.02% near 1 μm, effectively increasing the transmission and laser damage thresholds of the crystal [14]. With the increase in laser power and channel aperture, the structure size of the crystal lens window becomes larger, which is more difficult to manufacture. The crystal material will absorb part of the laser energy and produce thermal deformation, thereby losing the beam quality, which limits the use of traditional solid windows. The researchers introduced a transverse stream of airflow to separate the environment, which uses high-pressure gas that expands through a nozzle to create a strong pressure gradient across the window. The existing transverse supersonic jet aerodynamic window structure is subdivided into windows with a homogeneous flow on the nozzle section and free-vortex windows. In [15], the authors examined producing jets with a uniform velocity distribution on the nozzle section; however, a considerable air mass flow rate was required. The change in the momentum in the jet because of the pressure difference was accompanied by the appearance of a shock wave and a rarefaction-wave fan, which resulted in deteriorating the quality of the optical beam. With the use of nozzles, they generated a velocity distribution corresponding to the free vortex on the nozzle section, which could preserve the beam mass [16,17]. The design of a supersonic free-vortex aerodynamic window ensuring optical quality and fluid-mechanical sealing of a simulated laser cavity for active controlling of the gas flow in the aerodynamic window by adjusting part of the diffuser has been discussed [18]. The mathematical models and computational tools for designing, analyzing, and predicting the supersonic jet and nozzle flow in the aerodynamic windows of high-power gas lasers have been considered. A nozzle contouring tool was developed, offering the possibility to solve the problem of the aerodynamic design of nozzle devices with specified characteristic flows [19,20]. In the problem of sealing the large-aperture channel for high-power laser transmission, it is necessary to consider the small volume flow of the outlet of the air purification equipment. Accordingly, as the aperture of the channel increases, the velocity of the purge gas becomes much less than the speed of sound. In addition to achieving the window sealing of the channel, the sealing solution should also alleviate the problem of thermal effects in the channel because of the partial absorption of laser energy by the gas and optical elements.

In this study, three aerodynamic window sealing schemes of axial blowing, radial blowing, and axial–radial blowing are proposed for a large-aperture channel. Under the condition of a constant volume in the flow of purge gas, numerical models for the gas and dust particle movement in the large-aperture channel are established for different blowing schemes based on the hydrodynamic equation and particle motion equation. Moreover, the z-directional wind speed and dust particle mass concentration of the monitoring surface in the channel are used as indicators. In this study, the effect of radial blowing position on the sealing performance of the axial–radial blowing scheme is first analyzed before comparing the sealing performance of three blowing schemes. Thereafter, the sealing capacity of the axial blowing scheme with the best sealing performance is predicted. Finally, the accuracy of the analysis is experimentally verified.

2. Theory Model

The high-power laser emission system carries air purification equipment, which filters out most of the water and dust particles in the air to obtain a dry and clean gas with a very low heat absorption coefficient. The purge gas can be considered a viscous fluid with constant density, and the flow field in the channel is considered an incompressible field. The incompressible viscous gas hydrodynamic equations for the numerical analysis of the fluid in a large-aperture channel are expressed as [21]:

$$\nabla \cdot \vec{v} = 0 \tag{1}$$

$$\frac{\partial \vec{v}}{\partial t} + \left(\vec{v} \cdot \nabla\right)\vec{v} = \vec{F} - \frac{1}{\rho}\nabla p + \frac{\mu}{\rho}\nabla^2 \vec{v} \tag{2}$$

where $\vec{v}$ indicates the velocity vector, $\vec{F}$ denotes the external force per unit volume, and μ indicates the dynamic viscosity.

The motion of the discrete phase of the dust particles is solved by the equation of balance of forces, which are expressed as [22]:

$$\frac{du_p}{dt} = F_D\left(u_f - u_p\right) + \frac{g\left(\rho_p - \rho\right)}{\rho_p} + F_p \tag{3}$$

$$F_D = \frac{18\mu}{\rho_p d_p^2}\frac{C_D \mathrm{Re}}{24} \tag{4}$$

$$\mathrm{Re} = \frac{\rho d_p \left|u_p - u_f\right|}{\mu} \tag{5}$$

$$C_D = 0.22 + \frac{24}{\mathrm{Re}}\left[1 + 0.15\mathrm{Re}^{0.6}\right] \tag{6}$$

where u_f denotes the fluid speed, u_p corresponds to the particle speed, ρ_p symbolizes the particle density, d_p indicates the particle diameter, C_D denotes the traction coefficient, and F_p refers to the other force on the dust particle.

It is assumed that ambient air comprises ambient gas and dust particles. The high-power laser transmitted in the channel is a collimating Gauss light beam with a waist radius of 50 mm. To avoid the influence of the channel on the beam, a large-aperture channel with an outer diameter of 160 mm and an inner diameter of 154 mm was selected. Three blowing schemes modeled to achieve large-aperture channel sealing using the incompressibility of the purge gas are presented in Figure 1. Figure 1a illustrates that the channels are connected using a dynamic sealing structure, and that the mirrors are installed at the corners of the channels so that the laser can freely change the beam direction by transmitting in the rotating channels. Moreover, the air purification equipment output volume flow of purge gas is certain, and the gas has three transmission paths. First, via the axial blowing directly into the large-aperture channel; second, via the guide tube radial blowing to the large-aperture channel port; third, via simultaneous axial blowing and radial blowing. Figure 1b,c show the structure and location of the radial blowing scheme outlet. If radial blowing is required to seal the large-aperture channel, the width of the airflow must be greater than 160 mm. To leave a margin for airflow width, we chose to use nine guide tubes with an outer diameter of 20 mm. At the same time, the cuboid pipe of 180 × 180 × 20 mm in size was connected to the outlet of the guide tube so that the gas flowed out from the other side of the cuboid pipe more evenly.

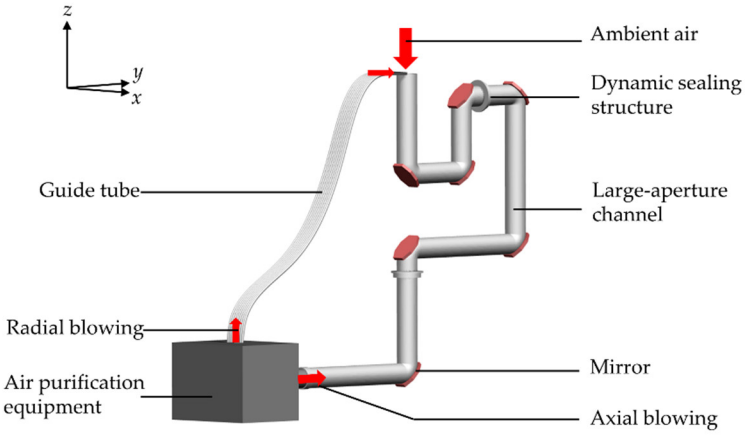

(**a**)

Figure 1. *Cont.*

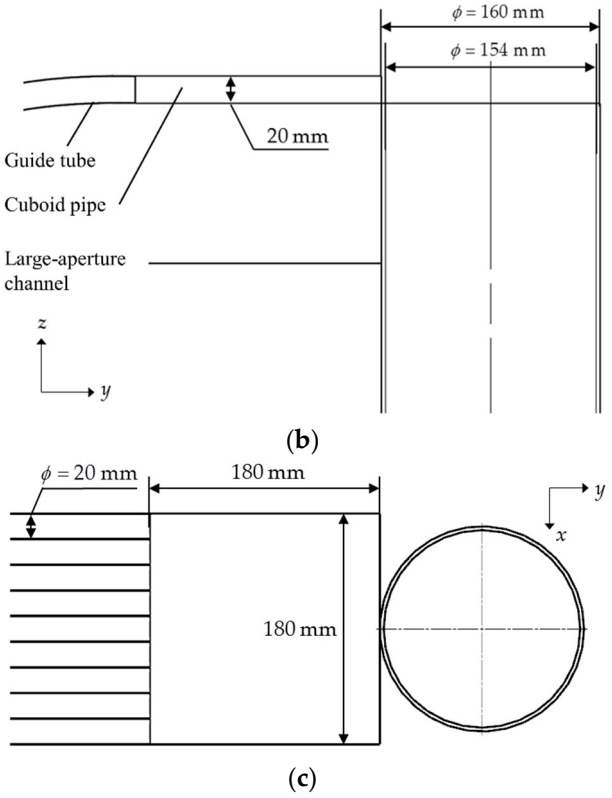

Figure 1. Three blowing scheme models for large-aperture channel sealing. (**a**) The overall structure scheme model; (**b**,**c**) the structure and location of the outlet of the radial blowing scheme.

3. Numerical Simulation

We used ANSYS software to simulate the motion of gas and dust particles under three different blowing schemes. A larger volume of cylindrical extension domain was added at the channel port to simulate the effect of the external environment on the large-aperture channel. The structure of the large-aperture channel is complex, and the calculation of the flow field and the discrete phase in the channel should be considered. The coupling analysis of high-power laser and flow field will become the focus of future research. To ensure the efficiency and accuracy of the calculation, the finite volume method is used to discretize the computational domain space. At the same time, the SIMPLE algorithm is used to solve the governing equations of each volume element. During the numerical simulation, we assumed that the gas normal and tangential velocities are zero at the fluid-solid interface. Any change in the motion of the gas will not affect infinity. Furthermore, on both sides of the interface of different gases, the gases have equal normal and tangential velocities and stresses. The fluid simulation model of the large-aperture channel is shown in Figure 2. Figure 2a presents a schematic diagram of the model boundary conditions. It can be observed that there are three gas inlets in the channel, and the corresponding faces are set as the velocity inlet boundary. Among them, v_a indicates the purge gas speed in the axial blowing scheme, v_r denotes the purge gas speed in the radial blowing scheme, and v_{out} indicates the velocity of ambient gas and dust particles. Notably, it is assumed that the velocity of dust particles moving in the environment is equal to the wind speed. In the axial blowing scheme, the v_r blowing device is removed. The outlet area of the channel is integrated with the cylindrical extension domain, and the bottom surface of the cylindrical extension domain is set as the outflow boundary. The inner wall of the channel is considered the non-slip static wall. The cylindrical surface of the extension domain is set as the symmetry boundary. Suppose that the z-coordinate of the end face of the channel outlet is Z_1, the z-coordinate of the monitoring surface is Z_2, and the z-coordinate of the end face position at the bottom of the radial blowing is Z_3. Accordingly, $L = Z_1 - Z_2$

and $l = Z_3 - Z_1$, where L denotes the monitoring distance and l denotes the radial wind distance. The relative position of the coordinates is shown in Figure 2b.

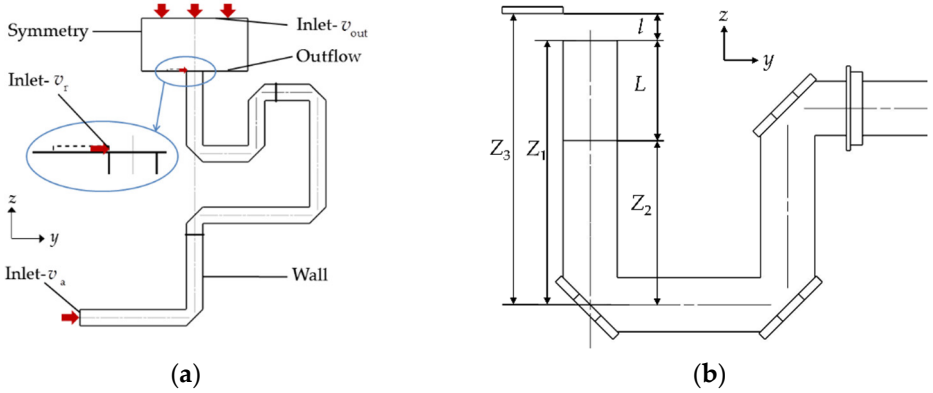

(**a**) (**b**)

Figure 2. Fluid simulation model of the large-aperture channel. (**a**) The schematic diagram of the model boundary conditions; (**b**) the monitoring distance and the radial wind distance location diagram.

The environmental conditions of the numerical simulation are consistent with the experimental, which helps to better compare with the experimental data. The environmental conditions of the numerical model are: (1) The volume flow of purge gas at the outlet of air purification equipment is 0.03 m^3/s; (2) the wind speed of the external environment is 6 m/s; (3) the mass concentration of the ambient dust particles is 6.32×10^{-8} kg/m^3; (4) the minimum diameter of the ambient dust particles is 0.3 μm, the maximum diameter is 10 μm, the average diameter is 1.8 μm, and the propagation coefficient is 0.553. When comparing different blowing scheme models, the change from the axial to the radial blowing mode is the problem of purge gas volume flow distribution. According to the conditions of axial and radial blowing cross-sectional area and volume flow of purge gas, the value range of axial wind speed v_a is 0–1.6 m/s. Therefore, it can be considered that the radial blowing scheme is $v_a = 0$ m/s, the axial blowing scheme is $v_a = 1.6$ m/s, and the axial–radial blowing scheme is 0 m/s $< v_a <$ 1.6 m/s. From the section size of each inlet and the gas velocity, it can be known that the fluid motion state is turbulent. The turbulent intensity of each inlet will change with the gas velocity. In Reynolds-Averaged Navier–Stokes (RANS) turbulence models, we use the standard $k - \varepsilon$ two-equation model to analyze the gas motion.

3.1. Numerical Simulation Modeling of Three Blowing Schemes

The last mirror in the large-aperture channel is positioned 700 mm from the exit section. It is necessary to ensure that the sealing requirements are met at a monitoring distance of $L \geq 100$ mm to avoid the influence of the external environment on the optical components. Therefore, multiple monitoring surfaces are established at the position of $L < 100$ mm with v_z and c as indicators, where v_z indicates the minimum non-zero z-directional wind speed of the monitoring surface and c indicates the maximum particle mass concentration of the monitoring surface. If $v_z < 0$ m/s or $c > 0$ kg/m^3, it is considered that the position cannot be sealed for the large-aperture channel. It should be mentioned that different values of l and v_a will impact the sealing performance of the large-aperture channel in the axial–radial blowing scheme.

For example, consider testing the sealing performance of the large-aperture channel at the $L = 20$ mm position. First, the schemes of axial blowing, radial blowing, and axial–radial blowing ($l = 0$ mm) are established for the large-aperture channel. We set the turbulent intensity at the inlet-v_{out} to 0.032 and the hydraulic diameter to 1000 mm. In the axial blowing scheme, we set $v_a = 1.6$ m/s, $v_r = 0$ m/s, $v_{out} = 6$ m/s, and the turbulent intensity at the inlet-v_a to 0.047 and the hydraulic diameter to 154 mm. In the radial blowing scheme, we set $v_a = 0$ m/s, $v_r = 8.3$ m/s, $v_{out} = 6$ m/s, and the turbulent intensity at the inlet-v_r to 0.046 and the hydraulic diameter to 36 mm. In the axial–radial blowing scheme, we set $v_a = 1$ m/s, $v_r = 3.2$ m/s, $v_{out} = 6$ m/s, the turbulent intensity

at the inlet-v_a to 0.05 and the hydraulic diameter to 154 mm, and the turbulent intensity at the inlet-v_r to 0.052 and the hydraulic diameter to 36 mm. Following the numerical simulation, the velocity vector of $x = 0$ mm section and the z-directional wind speed and particle mass concentration of the $L = 20$ mm monitoring surface are obtained, as shown in Figure 3. It can be observed that the wind speed in the large-aperture channel is different for different blowing schemes. At $L = 20$ mm, the $v_z > 0$ m/s of the axial blowing and axial–radial blowing scheme prove it can resist the ambient gas blowing in; however, with the $v_z < 0$ m/s of the radial blowing scheme, it is obvious that there is ambient gas blowing into the large-aperture channel. The $c \neq 0$ kg/m^3 for the three blowing schemes illustrates that none of the three blowing schemes can achieve a seal on the dust particles at this monitoring distance.

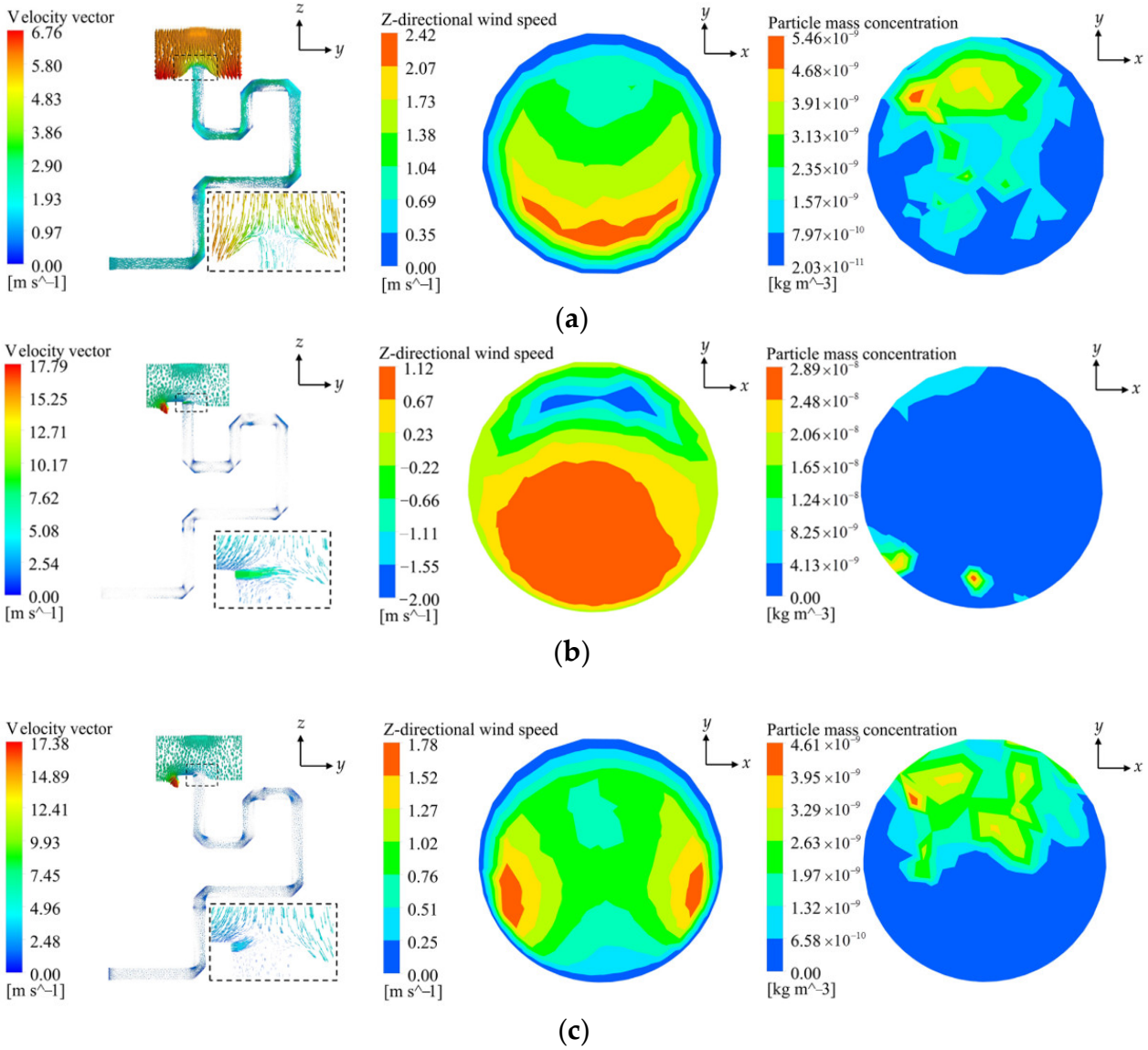

Figure 3. Velocity vector of section $x = 0$ mm, and the z-directional wind speed and particle mass concentration of $L = 20$ mm monitoring surface for the large-aperture channel under the three blowing schemes. (**a**) Axial blowing; (**b**) radial blowing; (**c**) axial–radial blowing ($l = 0$ mm, $v_a = 1$ m/s).

3.2. Comparison of Sealing Performance of Three Blowing Schemes

Since the axial blowing and the radial blowing scheme is fixed, while the axial–radial blowing scheme has a variety of l and v_a options, it is important to choose the scheme

with the best parameters in the axial–radial blowing scheme to compare with the other two blowing schemes. Using the control variable method, the effect of the variation of the l value in the axial–radial blowing scheme on the channel sealing performance is first analyzed. When the axial wind speed $v_a = 1$ m/s, the variation curves of sealing indicators for the large-aperture channel with different l are shown in Figure 4. More specifically, Figure 4a illustrates the v_z variation curves with L for different l. Evidently, v_z is greater than 0 m/s at $L > 20$ mm in all six curves with different l, indicating that the ambient gas can be stopped from blowing in. When $L < 60$ mm, the v_z of $l = 0$ mm curve is always positive, and when $L \geq 60$ mm, the curves of different l tend to be stable and slightly different. Figure 4b presents the c variation curves with L for different l. It can be observed that the c of different l curves gradually converge to a stable value with the increase of L. At $L = 80$ mm, c is reduced to zero, so the dust particles can be stopped from blowing in. However, at $L < 80$ mm, the c of $l = 0$ mm curve is the smallest. Generally, for different radial wind distance l, when the monitoring distance $L > 80$ mm, the large-aperture channel can stop both ambient gas and dust particles from blowing in, thereby achieving a good sealing effect. However, at different monitoring distances, the $l = 0$ mm curve can always maintain $v_z > 0$ m/s, c is minimum, and the curve stabilizes at the fastest rate. Therefore, among the six different l values, the sealing performance is relatively better when $l = 0$ mm.

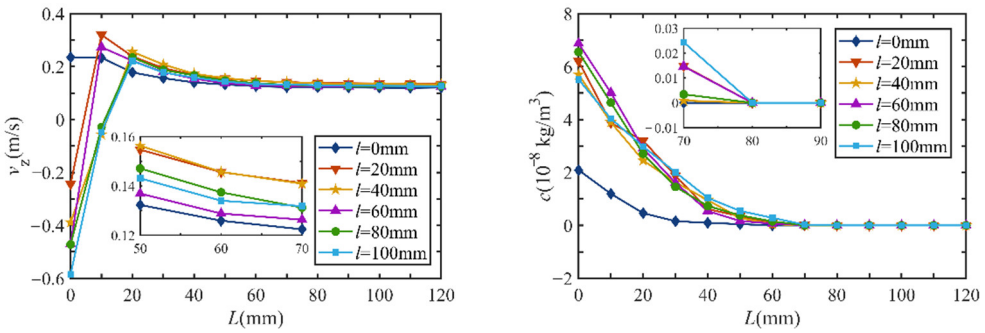

Figure 4. Variation curves of sealing indicators for the large-aperture channel with different l when $v_a = 1$ m/s. (**a**) The v_z variation curves with L for different l; (**b**) the c variation curves with L for different l.

The axial–radial blowing scheme at $l = 0$ mm is considered to compare the sealing performance with the other two blowing schemes. The variation curves of the sealing indicators for the large-aperture channel with different v_a are shown in Figure 5 to better analyze and compare the sealing performance of the three blowing schemes. Figure 5a illustrates the v_z variation curves with L for different v_a. It can be observed that at the same L position, v_z increases when v_a increases. When $v_a \geq 0.8$ m/s, v_z gradually stabilizes with the increase of L, and they are all greater than 0 m/s after $L > 20$ mm. In other words, the large-aperture channel can achieve the sealing of the ambient gas. Figure 5b depicts the c variation curves with L for different v_a. It can be observed that c converges to a stable value faster as v_a increases. When $v_a \geq 0.8$ m/s and $L \geq 80$ mm, all c values decrease to 0 kg/m^3. It indicates that the large-aperture channel can achieve the sealing of dust particles. In conclusion, the larger the axial wind speed v_a, the better the sealing effect of the large-aperture channel on the ambient gas and dust particles. Therefore, the axial blowing scheme is the best choice for aerodynamic window sealing.

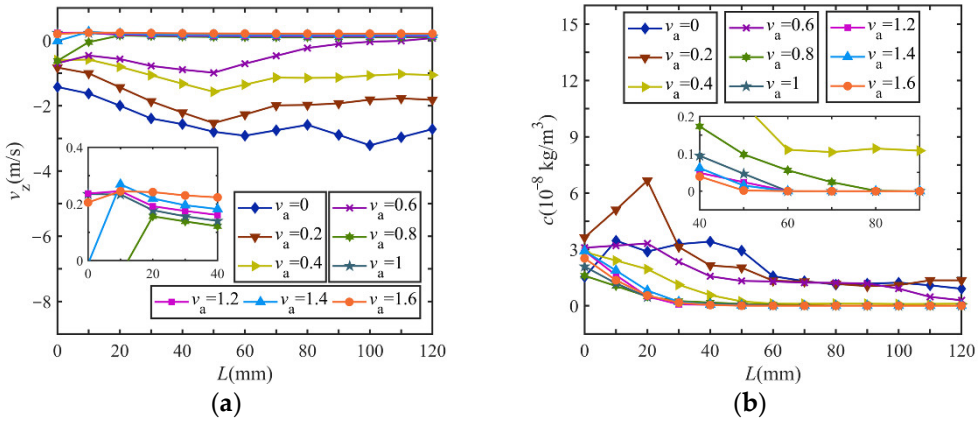

(**a**) (**b**)

Figure 5. Variation curves of the large-aperture channel sealing indicators for three blowing schemes. (**a**) The v_z variation curves with L for different v_a; (**b**) the c variation curves with L for different v_a.

3.3. Prediction of Window Sealing Performance for Axial Blowing Scheme

As shown in the previous section, when the ambient gas wind speed is 6 m/s, and the dust particle mass concentration is 6.32×10^{-8} kg/m^3, the axial blowing scheme effectively seals the large-aperture channel; however, sometimes, high-power laser emission systems are used in harsh environments. Therefore, the design requirement of the aerodynamic window sealing scheme is: that in the environment of seven-force wind (13.9–17.1 m/s) and sandstorm (4×10^{-3} kg/m^3), the large-aperture channel can resist ambient gas and dust particles entering the sealing area. That is, when the ambient wind speed is less than 18 m/s, and the dust particle mass concentration is less than 4×10^{-3} kg/m^3, the minimum non-zero z-directional wind speed of the monitoring surface is $v_z > 0$ m/s at the position where the monitoring distance $L = 100$ mm; and the maximum particle mass concentration $c = 0$ kg/m^3.

The axial blowing scheme is used as the aerodynamic window to seal the large-aperture channel. The sealing performance is primarily related to the ambient wind speed and dust particle mass concentration. Therefore, the sealing performance of the axial blowing scheme is predicted from two perspectives. The first: under the assumption that the ambient dust particle mass concentration is 4×10^{-3} kg/m^3, the minimum non-zero z-directional wind speed v_z variation curves with the monitoring distance L at v_{out} of 14 m/s, 16 m/s, 18 m/s, 20 m/s, 22 m/s, and 24 m/s is analyzed as shown in Figure 6. It can be observed that the larger the v_{out}, the smaller the v_z at the same monitoring distance position, and the curve stabilizes more slowly. However, at $L = 60$ mm, the v_z of all curves can fundamentally stabilize in some positive range. At different v_{out} values, the pressure distribution at the $x = 0$ mm section position of the large-aperture channel is shown in Figure 7, where Figure 7a illustrates $v_{out} = 14$ m/s and Figure 7b shows $v_{out} = 24$ m/s. When comparing the two figures, it is clear that despite the large difference in ambient wind speed, the relative positive pressure can be consistently maintained inside the large-aperture channel to the external environment, and the ambient gas cannot be blown into the deeper position of the channel, but only from channel port around the outflow. Therefore, the larger the v_{out}, the smaller the pressure at the outlet. Combining Figures 6 and 7, the axial blowing scheme can achieve sealing for the wind speed of 24 m/s or even greater in the sealing area of $L \geq 100$ mm for the continuous phase of the ambient gas.

Second, with v_{out} and c_{out} as variables, where c_{out} denotes the ambient dust particle mass concentration, we analyze whether the axial blowing scheme can achieve the sealing of the discrete phase of dust particles for the area of channel mm under different dust particles velocities and mass concentration environments. Let v_{out} be three wind speed levels of 20 m/s, 22 m/s, and 24 m/s, and c_{out} be eight mass concentration levels equally divided between 1×10^{-3} and 8×10^{-3} kg/m^3. The variation curve of the maximum particle mass concentration c with ambient dust particle mass concentration c_{out} at the

position of channel monitoring distance $L = 100$ mm for different v_{out} is shown in Figure 8. It can be seen that when $v_{out} = 22$ m/s and $c_{out} = 2 \times 10^{-3}$ kg/m^3, the situation of $c > 0$ kg/m^3 appears; and as v_{out} increases, the increase of c is more obvious. When $v_{out} = 24$ m/s, c is even greater than 2×10^{-6} kg/m^3 appears, and the pollution of the channel sealing area is serious. When $v_{out} = 20$ m/s, c is always zero. Therefore, the axial blowing scheme can achieve the sealing of dust particles in the large-aperture channel in environments where $v_{out} \leq 20$ m/s and $c_{out} \leq 8 \times 10^{-3}$ kg/m^3.

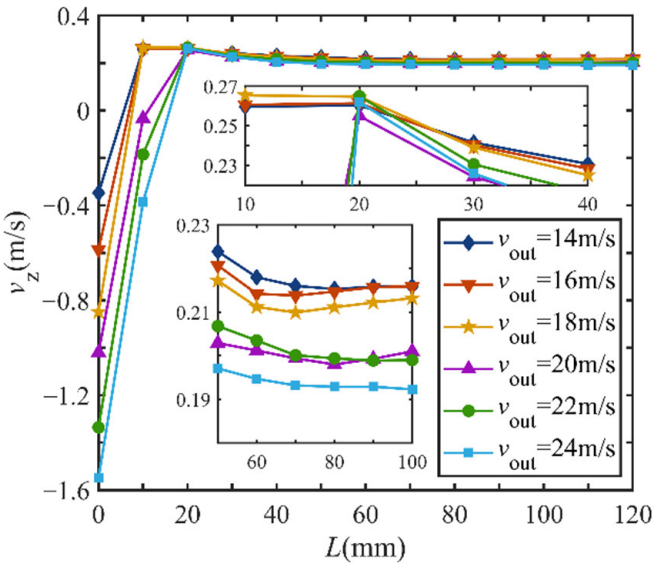

Figure 6. Variation curves of v_z with L for different v_{out}.

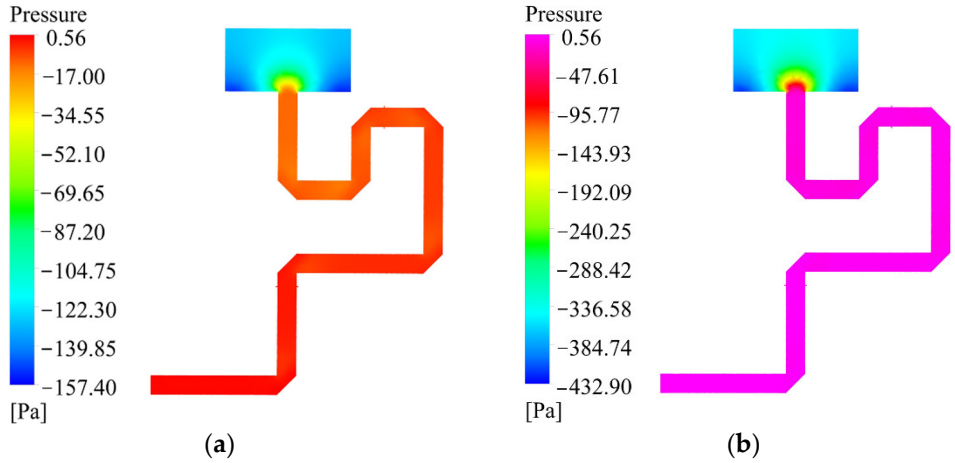

Figure 7. Pressure distribution at the $x = 0$ mm section position of the large-aperture channel at different v_{out}. (**a**) $v_{out} = 14$ m/s; (**b**) $v_{out} = 24$ m/s.

In summary, the sealing performance of the axial blowing scheme on the gas continuous phase is much greater than that of the dust particle discrete phase. Therefore, the most crucial factor determining the sealing performance is whether the dust particle can be sealed. The velocity of the ambient dust particles has a more significant impact on the channel sealing effect than the mass concentration. For the same particle, the faster the velocity, the more kinetic energy the particle can transfer to the deeper part of the channel. In the environment of $v_{out} \leq 20$ m/s and $c_{out} \leq 8 \times 10^{-3}$ kg/m^3, the axial blowing scheme can simultaneously achieve the sealing of ambient gas and dust particles in the large-aperture channel. It is proved that the aerodynamic window satisfies the sealing design requirements in a class 7 wind (13.9–17.1 m/s) and sandstorm (4×10^{-3} kg/m^3) environment.

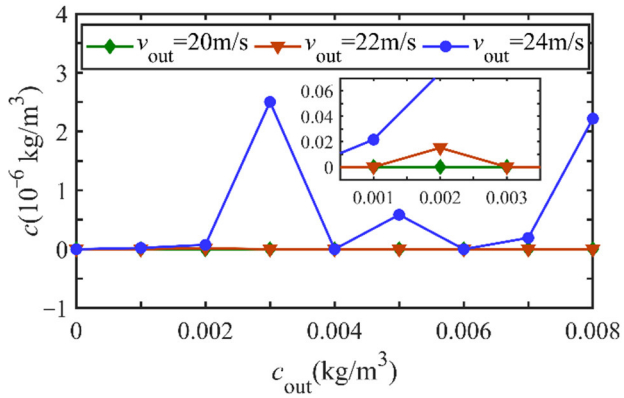

Figure 8. Variation curves of c with c_{out} at the position of $L = 100$ mm for different v_{out}.

4. Experimental Verification

The seal test experiments for the large-aperture channel were performed in a laboratory environment, and the experimental platform was fabricated, as shown in Figure 9. Fan blowing was used to simulate the ambient wind speed, and the maximum fan gear speed was approximately 6 m/s. The number of particles of different particle diameters in the channel was measured using an airborne particle counter, and the gas speed in the channel was measured using a heated thermometer anemometer. In the axial blowing scheme, we opened the axial blowing valve and closed the radial blowing valve, and then turned on the air purification equipment and fan. After the flow field in the channel reached stability, the heated thermometer anemometer was used to measure the wind speed at 12 points in the channel $L = 20$ mm, and the distribution of the point locations is shown in Figure 10. The wind speed at each point was measured through three experiments, and the average value was compared with the simulated data, as shown in Table 1. It is evident that the experimentally measured values are slightly larger than the simulation results, which are considered to be caused by the instability of the purge gas volume flow, external environmental factors, manual measurement errors, and instrumentation errors. Fundamentally, in the Y direction, the wind speed increases with the decrease in the Y coordinate, and in the X direction, it is basically symmetrical around the center of the monitoring surface. The velocity distribution law is the same as the simulation results, which proves that the numerical simulation model of the channel is accurate, and the numerical model can be used to analyze and study the sealing effect of the large-aperture channel to the ambient gas.

Figure 9. Large-aperture channel sealing experimental model.

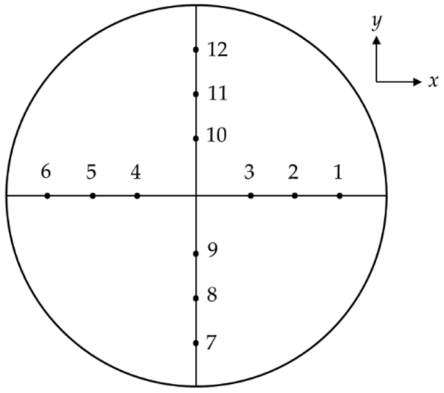

Figure 10. Distribution of wind speed measurement points inside the large-aperture channel.

Table 1. Experimental and simulation data of wind speed at the measurement point.

Location	Experiment (m/s)	Simulation (m/s)	Location	Experiment (m/s)	Simulation (m/s)
1	1.38	1.32	7	2.51	2.34
2	1.62	1.54	8	1.86	1.78
3	1.41	1.34	9	1.48	1.46
4	1.36	1.27	10	1.16	1.14
5	1.59	1.46	11	1.03	0.92
6	1.61	1.36	12	1.02	0.82

Based on the previous wind speed test experiment, we carried out the first group of the number of particles measurement experiments. We opened the radial blowing valve and controlled $v_a = 1$ m/s. After the flow field reached stability in the channel, the number of particles at different L was measured three times with the airborne particle counter under the condition of multiple l values. After completing the statistics, we conducted the second group of the number of particles measurement experiments. The radial blowing was fixed at $l = 0$ mm. We changed the value of v_a by adjusting the axial and radial blowing valves. After the flow field reached stability in the channel, the number of particles at different L was measured three times using the airborne particle counter. The number of particles of different particle diameters in the channel was used to calculate the value of c_m, where c_m indicates the mean particle mass concentration of the monitoring surface. The c_m variation curves of the large-aperture channel for the experimental measurement of the different blowing scheme are presented in Figure 11. Figure 11a depicts the c_m variation curves with L for different l. It can be observed that each curve c_m tends to a stable value at $L > 80$ mm. However, the purge gas also contains a few dust particles, the stable value is not zero. It can be proved that the channel prevents the dust particles from blowing in. Moreover, the c_m of the $l = 0$ mm curve is relatively small and stabilizes at $L = 60$ mm with the fastest stabilization rate, indicating the best sealing performance at this location. Figure 11b displays the c_m variation curves with L for different v_a. It can be observed that when $v_a \geq 0.8$ m/s and $L > 80$ mm, c_m eventually converges to a stable value. As v_a becomes larger, the c_m value stabilizes faster, and the c_m value at the same L position grows smaller. When $v_a = 1.6$ m/s, c_m stabilizes the fastest and is the smallest value until stabilization. It shows that the axial blowing scheme is indeed the best choice for the aerodynamic window.

In the numerical simulation analysis, we assume that c indicates the maximum particle mass concentration of the monitoring surface. In the experimental data analysis, we assume that c_m indicates the mean particle mass concentration of the monitoring surface. As c_m and c indicate different meanings, we demonstrate the accuracy of the numerical model by comparing the relative size and trend of the curves. The comparison curves between experimental and simulation data are presented in Figure 12, where the c variation curves represent the simulation data and the c_m variation curves denote the experimental data. Figure 12a depicts the c_m and c variation curves with L for different l. It can be observed

that there are some differences in the relative magnitude of the $l = 20$ mm curve, which are considered to be caused by the instability of the purge gas volume flow and manual measurement errors. When $l = 0$ mm, the c_m and c values remain relatively small, and the curves stabilize at the fastest rate. Figure 12b displays the c_m and c variation curves with L for different. It can be observed that when $v_a < 0.8$ m/s, c_m and c do not reach a stable value. When $v_a \geq 0.8$ m/s, c_m and c eventually converge to a stable value. As v_a becomes larger, the c_m and c values stabilize faster. Therefore, by analyzing Figure 12a,b, it is clear that the relative magnitudes and trends of the curves of the experimental and simulated data are consistent. The experimental conclusion is the same as the simulation result, which proves the accuracy of the numerical simulation model established for the large-aperture channel.

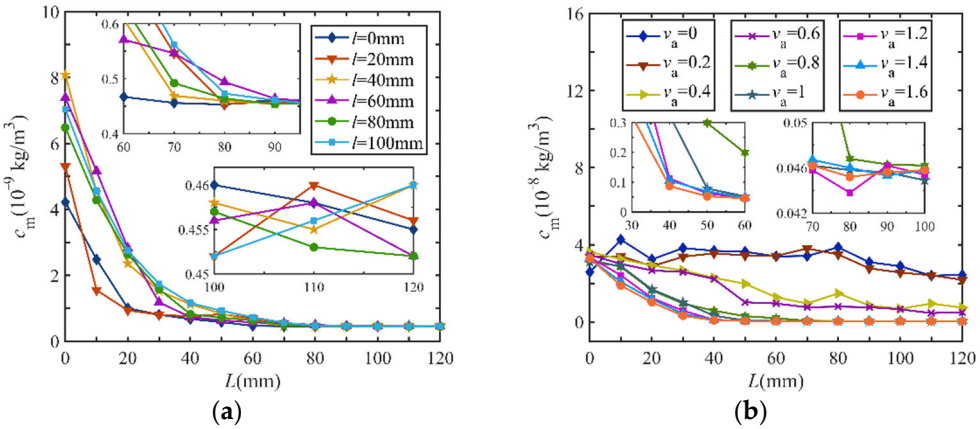

Figure 11. Variation curves of c_m of the large-aperture channel for the experimental measurement of the different blowing scheme. (**a**) The c_m variation curves with L for different l; (**b**) the c_m variation curves with L for different v_a.

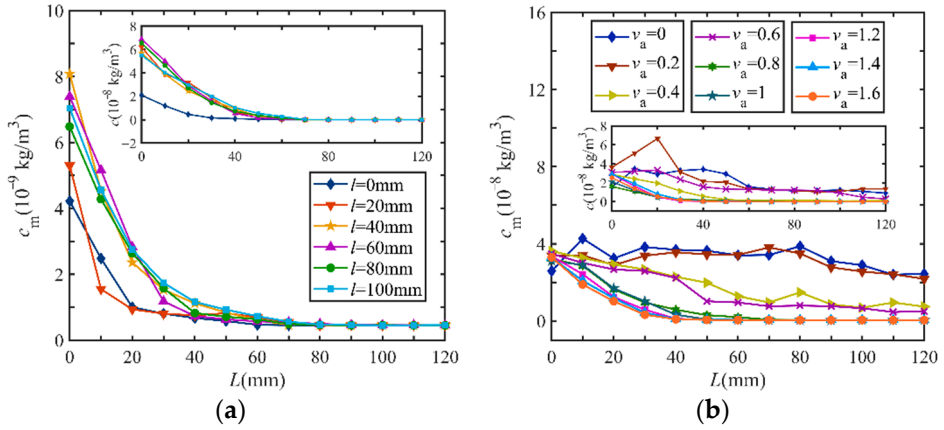

Figure 12. Comparison curves between experimental and simulation data. (**a**) The c_m and c variation curves with L for different l; (**b**) The c_m and c variation curves with L for different v_a.

5. Conclusions

In this study, the sealing problem of the large-aperture channel for high-power laser transmission was analyzed numerically via a simulation and also experimentally. Based on the usage conditions of the large-aperture channel, three schemes of axial blowing, radial blowing, and axial–radial blowing are proposed as aerodynamic windows for channel sealing. First, the influence of the radial wind distance l on the sealing performance of the axial–radial blowing scheme is analyzed. Accordingly, the smaller the l is, the better the ability of the channel to resist the intrusion of the ambient gas and dust particles, and the large-aperture channel can achieve a better sealing effect. Furthermore, in the comparison

of the sealing performance of the three blowing schemes, it was found that the minimum non-zero z-directional wind speed and dust particle mass concentration can reach a stable value at a shorter monitoring distance inside the large-aperture channel with a larger proportion of purge gas volume flow in the axial direction. Moreover, the relative size and variation trend of the simulation data are consistent with the experimental results. Finally, when predicting the sealing performance of the axial blowing scheme, it was found that under the condition of an ambient wind speed of 24 m/s or even greater, the large-aperture channel can always maintain relatively positive pressure and effectively block the continuous phase of ambient gas blowing in. Dust particles have a certain initial kinetic energy, so dust particles are the decisive factor in determining the sealing performance, and the velocity of dust particles affects the sealing effect of the channel more than the mass concentration. The research results theoretically support the aerodynamic window sealing scheme for large-aperture channels, paving the way for the wide application of high-power lasers.

Author Contributions: Formal analysis, Y.W.; Resources, S.S.; Supervision, Y.S.; Writing—original draft, X.H. All authors have read and agreed to the published version of the manuscript.

Funding: This research was funded by Laser Ranging Detector, grant number E12701SZCZ00.

Institutional Review Board Statement: Not applicable.

Informed Consent Statement: Not applicable.

Data Availability Statement: Not applicable.

Conflicts of Interest: The authors declare no conflict of interest.

References

1. Zuo, J.; Lin, X. High-Power Laser Systems. *Laser Photon-Rev.* **2022**, *16*, 2100741. [CrossRef]
2. Cook, J. High-energy laser weapons since the early 1960s. *Opt. Eng.* **2012**, *52*, 021007. [CrossRef]
3. Extance, A. Military technology: Laser weapons get real. *Nature* **2015**, *521*, 408–410. [CrossRef] [PubMed]
4. Zhang, Y.; Ji, X.; Li, X.; Yu, H. Thermal blooming effect of laser beams propagating through seawater. *Opt. Express* **2017**, *25*, 5861–5875. [CrossRef] [PubMed]
5. Fischer, R.; Ting, A.; DiComo, G.; Prosser, J.; Peñano, J.; Hafizi, B.; Sprangle, P. Absorption and scattering of 106 μm laser radiation from oceanic aerosols. *Appl. Opt.* **2009**, *48*, 6990–6999. [CrossRef] [PubMed]
6. Lu, L.; Wang, Z.; Zhang, P.; Qiao, C.; Cai, Y. Thermal blooming induced phase change and its compensation of a Gaussian beam propagation in an absorbing medium. *Opt. Lett.* **2021**, *46*, 4304–4307. [CrossRef] [PubMed]
7. Yang, L.; Xiang, X.; Miao, X.; Li, Z.; Li, L.; Yuan, X.; Zhou, G.; Lv, H.; Zu, X. Influence of oil contamination on the optical performance and laser induced damage of fused silica. *Opt. Laser Technol.* **2015**, *75*, 76–82. [CrossRef]
8. Raman, R.N.; Demos, S.G.; Shen, N.; Feigenbaum, E.; Negres, R.A.; Elhadj, S.; Rubenchik, A.M.; Matthews, M.J. Damage on fused silica optics caused by laser ablation of surface-bound microparticles. *Opt. Express.* **2016**, *24*, 2634–2647. [CrossRef] [PubMed]
9. Génin, F.Y.; Feit, M.D.; Kozlowski, M.R.; Rubenchik, A.M.; Salleo, A.; Yoshiyama, J. Rear-surface laser damage on 355-nm silica optics owing to Fresnel diffraction on front-surface contamination particles. *Appl. Opt.* **2000**, *39*, 3654–3663. [CrossRef] [PubMed]
10. Bayya, S.S.; Chin, G.D.; Sanghera, J.S.; Aggarwal, I.D. Germanate glass as a window for high energy laser systems. *Opt. Express* **2006**, *14*, 11687–11693. [CrossRef] [PubMed]
11. Anoikin, E.; Muhr, A.; Bennett, A.; Twitchen, D.; de Wit, H. Diamond optical components for high-power and high-energy laser applications. *Compon. Packag. Laser Syst.* **2015**, *9346*, 172–180. [CrossRef]
12. Peng, Y.; Sheng, Z.; Zhang, H.; Fan, X. Influence of thermal deformations of the output windows of high-power laser systems on beam characteristics. *Appl. Opt.* **2004**, *43*, 6465–6472. [CrossRef] [PubMed]
13. Ye, X.; Huang, J.; Liu, H.; Geng, F.; Sun, L.; Jiang, X.; Wu, W.; Qiao, L.; Zu, X.; Zheng, W. Advanced Mitigation Process (AMP) for Improving Laser Damage Threshold of Fused Silica Optics. *Sci. Rep.* **2016**, *6*, 31111. [CrossRef] [PubMed]
14. Busse, L.E.; Florea, C.M.; Frantz, J.A.; Shaw, L.B.; Aggarwal, I.D.; Poutous, M.K.; Joshi, R.; Sanghera, J.S. Anti-reflective surface structures for spinel ceramics and fused silica windows, lenses and optical fibers. *Opt. Mater. Express* **2014**, *4*, 2504. [CrossRef]
15. Parmentier, E.M.; Greenberg, R.A. Supersonic Flow Aerodynamic Windows for High-Power Lasers. *AIAA J.* **1973**, *11*, 943–949. [CrossRef]
16. Guile, R.N.; Mapes, S.N.; Director, M.N.; Coulter, L.J. Performance of a multi-element centrifugal aerowindow. *AIAA Pap.* **1974**, 74–227.
17. Guile, R.; Hilding, W. Investigation of a free-vortex aerodynamic window. In Proceedings of the 13th Aerospace Sciences Meeting, Pasadena, CA, USA, 20 January–22 January 1975; p. 122. [CrossRef]

18. Wildermuth, E.; Giesen, A.; Hugel, H. Experimental Investigations of a Free-Vortex Aerodynamic Window. *Gas Flow Chem. Lasers* **1987**, *15*, 96–100. [CrossRef]
19. Volkov, K.N.; Pustovalov, A.V. Supersonic flows in channels and jets when applied to the problems of designing aerodynamic windows of gas lasers. *J. Eng. Phys. Thermophys.* **2015**, *88*, 1210–1220. [CrossRef]
20. Emelyanov, V.; Pustovalov, A.; Volkov, K. Supersonic jet and nozzle flows in uniform-flow and free-vortex aerodynamic windows of gas lasers. *Acta Astronaut* **2019**, *163*, 232–243. [CrossRef]
21. Wesseling, P. *Principles of Computational Fluid Dynamics*; Springer Science & Business Media: Berlin, Germany, 2009; Volume 29, pp. 1–643. [CrossRef]
22. Monaghan, J.J. Smoothed particle hydrodynamics. *Rep. Prog. Phys.* **2005**, *68*, 1703. [CrossRef]